Title: Multi-omic characterization of human sural nerves across polyneuropathies

Authors: Michael Heming[1†], Jolien Wolbert[1†], Anna-Lena Börsch[1], Christian Thomas[2], Anne K. Mausberg[3], I-Na Lu[1], Julia Tietz[1], Finja Dienhart[1], Christine Dambietz[1], Michael Müther[4], Anne-Kathrin Uerschels[5], Kathy Keyvani[6], Fabian Szepanowski[3], Bianca Eggert[3], Kai C. Liebig[3], Julieta Aprea[7], Andreas Dahl[7], Ruth Stassart[8], Robert Fledrich[9], Heinz Wiendl[1], Claudia Sommer[10], Mark Stettner[3], and Gerd Meyer zu Hörste[1*]

Affiliations:

1 Department of Neurology with Institute of Translational Neurology, Medical Faculty, University Hospital Münster, Münster, Germany
2 Institute of Neuropathology, University Hospital Münster, Münster, Germany
3 Department of Neurology, Center for Translational Neuro- and Behavioural Sciences (C-TNBS), University Hospital Essen, Essen, Germany
4 Department of Neurosurgery, University Hospital Münster, Münster, Germany
5 Department of Neurosurgery, University Hospital Essen, Essen, Germany
6 Department of Neuropathology, University Hospital Essen, Essen, Germany
7 DRESDEN-concept Genome Center, Center for Molecular and Cellular Bioengineering, Dresden University of Technology, Dresden, Germany
8 Paul-Flechsig-Institute of Neuropathology, University Hospital Leipzig, Leipzig, Germany
9 Institute of Anatomy, University of Leipzig, Leipzig, Germany
10 Department of Neurology, University Hospital Würzburg, Würzburg, Germany

†*These authors contributed equally*

**Corresponding author:* gerd.meyerzuhoerste@ukmuenster.de

Keywords: transcriptomics single cell RNA-seq, single-cell atlas, spatial transcriptomics, multi-omics, peripheral nervous system, polyneuropathies.

Abstract:

Diseases of peripheral nerves termed polyneuropathies (PNPs) are common, mechanistically heterogeneous, and challenging to diagnose, but have not been investigated at single cell resolution. Here, we integrated single nuclei transcriptomics of peripheral nerves from 33 human PNP patients and four controls (365,708 nuclei) with subcellular spatial transcriptomics. We identified and spatially validated novel and human-specific markers of myelinating and non-myelinating Schwann cells and unexpectedly heterogeneous perineurial fibroblasts. Nerve-associated leukocytes were diverse with an endoneurial to epineurial macrophage gradient. All PNPs shared a loss of myelinating and an increase in repair Schwann cells and lipid-associated macrophages. Transcriptional changes affected multiple cells outside of the endoneurium across PNPs, suggesting PNPs as 'pan-nerve diseases'. Spatially, PNPs showed a perineurial hyperplasia and fibrotic dispersion and this was most pronounced in immune-mediated PNPs. We found potential of single cell transcriptomics for supporting the differential diagnosis of PNPs and for their future unbiased diagnostic classification.

Significance Statement

The first large-scale integrated single cell and spatial transcriptomic characterization of human peripheral nerves identifies novel cell markers and unexpected heterogeneity of perineurial cells, reveals polyneuropathies as 'pan-nerve diseases', and shows that single cell transcriptomics hold potential for unbiased nerve disease classification.

Main Text:

Polyneuropathies (PNPs) generally denote diseases of multiple peripheral nerves and range among the most common neurological diseases, affecting at least 4% of the middle-age and elderly population(*1*). Patients affected by PNPs suffer from progressive sensory and motor impairment and an often painful life-long aggravating disease with an enormous socio-economic impact(*2*, *3*). The underlying causes of PNPs are very diverse and comprise diabetic, toxic inflammatory/immune-mediated, hereditary, metabolic and vitamin deficiency(*4–6*). Despite comprehensive diagnostic work-up, the underlying cause of PNPs remains unclear in many patients (20-30%)(*5*). Biopsy of the sensory sural nerve at the lateral ankle is often the final diagnostic step to assess specific causes in human PNP patients, but even biopsy does not lead to a diagnosis in many patients(*7*). This could be due to an insufficient depth of analysis of this tissue. Fully exploiting this precious biomaterial for mechanistic understanding and diagnostic potential is especially important to detect treatable causes such as immune mediated neuropathies, which account for up to 10% of the PNPs(*4*, *5*), and are treatable.

We and others previously performed single cell transcriptomic analyses of rodent peripheral nerves(*8–13*). This identified novel markers of endoneurial cells, unexpected complexity of hematopoietic cell types in peripheral nerves, and a transcriptional response to autoimmunity that was shared between the peripheral and central nervous system. However, human peripheral nerves have not been characterized using similar technologies. Whether the cellular composition and cell type markers are replicated cross-species has not been investigated yet. Moreover, it remains unknown how human nerve cells respond to PNPs

transcriptionally and compositionally on a single cell level and whether this is shared or distinct between PNP subtypes.

Here, by combining single nuclei and spatial transcriptomics of human sural nerve biopsies, we provide the first large-scale single cell atlas of human peripheral nerves. We defined the cellular micro-milieu in human peripheral nerves and detected a unique cellular composition of the perineurium and abundant nerve-associated leukocytes. We identified novel cell type markers of myelinating and non-myelinating Schwann cells (SC) and perineurial fibroblasts, which were validated spatially. Repair and damage SC, and occurrence of lipid-associated macrophages were shared features of PNPs. We also found that PNPs affected cells beyond the endoneurium, causing perineurial cell proliferation and perineurial thickening preferentially in inflammatory PNPs. Finally, patients could be categorized into patient clusters identified solely by single cell transcriptomics which hinted towards mechanistic patterning of patients. We thus provide a single cell atlas for the human peripheral nerve in health and PNPs and discover potential for an unbiased diagnostic classification of PNPs.

Results

Comprehensive species-specific single nuclei transcriptional atlas of human sensory nerves.

We here first created a large single cell transcriptomics atlas of human sural nerves of 37 donors (Fig. 1A). Sural nerves were collected in three centers from 33 PNP patients and four controls (Suppl. Fig. 1A; Suppl. Tab. 1). Control samples (CTRL) were residual material of surgical sural nerve autografts (‘interpositions’) from patients with traumatic nerve injuries, but unaffected by PNPs. We established protocols to extract nuclei of sufficient number and

quality and performed single nuclei RNA-sequencing (snRNA-seq) of all samples (Methods, Suppl. Fig. 1B, Suppl. Tab 2). After analytical removal of doublets and low quality nuclei and batch correction, this resulted in 365,708 total high-quality nuclei (Suppl. Fig. 1C-D, Suppl. Tab. 2). We then clustered the nuclei (henceforth termed 'cells' for simplicity) and annotated the clusters by using both predefined marker genes (Suppl. Fig. 2A, Suppl. Tab. 3) and automatic annotation based on rodent data(*9*, *10*, *14*) (Suppl. Fig. 2B). We identified endoneurial cell types including Schwann cells (*S100B, SOX10*), of both myelinating (mySC; *MPZ, MBP, PRX*) and non-myelinating (nmSC; *NCAM1*, *L1CAM, CDH2*) type and endoneurial fibroblast cells (endoC; *SOX9, PLXDC1, ABCA9*) (Fig. 1B, Supp. Fig. 2A). Schwann cells expressing features of damage (damageSC; *EGR1, FOS, JUN*) and of repair(*15*) (repairSC; *NGFR*, *ATF3, GDNF, RUNX2*) were also detected, which were not present in the reference rodent single cell data (*9*, *10*). Moreover, we found epineurial (epiC; *CCBE1, COMP*) and perineurial fibroblast cells (periC1-3; *SLC2A1*/GLUT1, *KRT19, CLDN1*) (Fig. 1B, Supp. Fig. 2A). This perineurial cell heterogeneity was greater than previously described in rodent single cell datasets (*8–10*, *12*). The periC3 cluster expressed genes markerassociated with extracellular matrix and collagen fibril organization, which distinguished it from the other two pericyte clusters (Suppl. Fig. 2B). Vascular cells included vascular smooth muscle cells (VSMC: *ACTA2*, *CARMN*), pericytes (PC1-2; *PDGRFB, RGS5*) and endothelial cells (EC; *EGFL7, PECAM1*) (Supp. Fig. 2A). Based on known markers (Suppl. Fig. 2A) and published reference scRNA-seq data(*14*) (Suppl. Fig. 2C) endothelial cells (EC) separated into lymphatic endothelial cells (LEC; *PROX1, LYVE1, FLT4*) and a venous (ven_EC: *PLVAP*, *ACKR1*) to capillary (capEC: *ABCG2*, *MFSD2A*) to arterial (artEC: *SEMA3G*, *HEY1*, *GJA5*) continuum. We identified a cluster of venous/capillary EC (ven_cap_EC2), which expressed blood-nerve barrier (BNB) markers *ABCB1* and

SLC1A1(16), blood-brain barrier marker *MFSD2A(17),* and tight junction transcript *GJA1* and therefore likely represented EC of the BNB (Fig. 1B, Supp. Fig. 2A). Nerve-associated leukocytes were mainly of myeloid lineage (Macro1: *MS4A7, CLEC10A;* Macro2: *MS4A7, CX3CR1*; Granulo: *S100A8, S100A9;* Mast: *CPA3, MS4A2*) outnumbering T/NK cells (T/NK: CD3E, *CD8A, NCR1, NKG7, GZMA*) and B cells (B: *CD79A, IGHM*) (Fig. 1B, Supp. Fig. 2A). We thus created a transcriptional cellular atlas of human peripheral nerves replicating and extending cell populations identified in single cell rodent studies(*8–13*).

We systematically compared cell type markers in humans with their published rodent counterparts(*8–10*) (Suppl. Tab. 4-6). As expected, the majority of cell marker transcripts were shared between species. However, several genes expressed in mySC (*MLIP*), nmSC (*GRIK3*, *PRIMA1*), and periC (*CXCL14*) have not been described in literature. When we re-analyzed published rodent datasets(*8–10*), we could detect *Mlip* in mySC in two of those(*9*, *10*), although they were not mentioned in the text (Fig. 1C, Suppl. Tab. 4-5). In contrast, *GRIK3*, *PRIMA1* and *CXCL14* , were not detectable at relevant levels (Suppl. Fig. 2D), which indicates that they could be specific for humans. We thus identified undescribed and species-specific transcripts in perineurial and Schwann cells in humans.

Spatially dissecting the human nerve ultrastructure confirms novel transcriptional cell type markers.

For morphological confirmation and characterization, we employed an *in situ* amplification-based spatial transcriptomics approach (Xenium; 'spatial-seq') to localize pre-defined transcripts at subcellular-resolution(*18*). We designed a custom panel of 99 RNA transcripts combining known (e.g., *PRX*) and novel (e.g., *GRIK3*) markers of nerve-associated cell types (Suppl. Tab. 7). Notably, highly transcribed genes such as myelin

protein-encoding genes (e.g. *MPZ*) had to be excluded to prevent optical overcrowding (Methods). We then visualized these RNA targets in a formalin-fixed paraffin-embedded (FFPE) cross-section of a human sural nerve graft (CTRL) with optimally maintained morphology.

First, we analyzed the overall cellular organization. By integrating spatial and snRNA-seq, each cell in spatial-seq was matched to a snRNA-seq cluster, which were aggregated into 8 larger groups (SC, endoC, periC, epiC, VSMC, PC, EC, IC), and then visualized spatially (Fig. 1D). As expected, each nerve consisted of multiple bundles (fascicles) formed by endoneurial cells (SC, endoC) and surrounded by a clearly demarcated layer of perineurial cells (periC). Vascular cell types (EC, VSMC, PC) formed vessels of either arterial, capillary, or venous morphology with EC forming the thin innermost layer (Fig. 1D). Epineurial cells (epiC) were located in between fascicles and were interspersed with immune cells that were rare in the endoneurial areas (Fig. 1D). We thus confirmed the snRNA-seq cluster annotation using spatial features. This also provides a histological annotation of peripheral nerve cells in an automated manner.

Second, when comparing periC and epiC transcripts identified in the snRNA-seq clusters, the previously undescribed perineurial markers (*CXCL14*) indeed co-localized with known perineurial fibroblast transcripts (*CLDN1, SLC2A1, KRT19*)(*11*) and outlined the perineurium (Fig. 1E). Among vascular cells, as predicted from snRNA-seq data, transcripts associated with epiEC (*PLVAP*) were located in vessels in the epineurium (Fig. 1F). In contrast, the BNB markers *ABCB1* and *SLC1A1,* expressed by the ven_capEC2 cluster in snRNA-seq, were enriched in endoneurial vessels together with known EC markers (*PECAM1, EGFL7*)(*11*, *19*) (Fig. 1F). This supports our interpretation that the ven_capEC2 cluster

represents cells of the BNB. Other vascular cell markers (e.g., *SEMA3G* in artEC) were preferentially associated with their respective vessel type (Suppl. Fig. 3A).

We then focussed on the human Schwann cell (SC) transcriptome. Known pan-SC markers (*SOX10, S100B, EGR2*)(*11*) were abundantly expressed across the endoneurium (Suppl. Fig. 3B). Known transcriptional markers of mySC (*PRX, CDH1, SLC36A2*)(*9*, *13*) co-localized with transcripts newly identified in the mySC cluster (*MLIP*) (Fig. 1G. and known transcriptional markers of nmSC (*L1CAM, CDH2, CHL1*)(*12*, *19*, *20*) co-localized with novel transcripts of the nmSC cluster (*PRIMA1, GRIK3*) (Fig. 1G). We thus spatially validated known and novel transcriptional markers of perineurial fibroblasts, the BNB, and human myelinating and non-myelinating Schwann cells.

Human peripheral nerves contain complex immune cells and replicate rodent macrophage heterogeneity.

We next sought to deeply characterize human nerve-associated immune cells. To capture the immune cell (IC) heterogeneity, we sub-clustered all leukocyte nuclei (n = 18,436) at high resolution (Fig. 2A). Clusters representing megakaryocytes/platelets (*PF4, GP9, PPBP*) and red blood cells (*HBA, HBB*) were undetected arguing against relevant blood contamination (Fig. 2A). The majority of IC clusters (79% of all IC nuclei) were of myeloid lineage with mainly macrophage annotation (Macro1-18: *LYZ*, *CD14*, *MRC1*, *CD163*, *MS4A7*) (Fig. 2A, Suppl. Fig. 4A, Suppl. Tab. 8). The transcriptional phenotype and ontogeny of nerve-associated macrophages in rodents differ depending on their endo- vs. epineurial location(*8*, *21*, *22*). When directly testing this in humans, macrophage clusters (*MS4A7*) exhibited a gradient of expression ranging from markers with known endoneurial (*CX3CR1, TREM2)* to epineurial (*LYVE1, FOLR2, TIMD4*) macrophage location in rodents (Fig. 2B).

When analyzing expression of a representative and tentatively endoneurial macrophage cluster (Macro18) its gene signature was enriched in lipid metabolism-related pathways (Fig. 2C). We next analyzed markers of epi- (*FOLR2*) vs. endoneurial (*CX3CR1*) macrophages (*MS4A7*)(*21*) in spatial transcriptomics. *CX3CR1* was preferentially detected endoneurial, although it was also present within epineurial vessels, and *FOLR2* was mostly located epineurial (Fig. 2D). We thus replicate the location-specificity of rodent nerve-associated macrophage phenotypes in humans. We additionally identified smaller myeloid clusters that could be assigned to classical dendritic cells (DC) type 1 (cDC1: *CLEC9A*, *XCR1*, *BATF3*), plasmacytoid DC (pDC: *CLEC4C*, *IRF8*), and classical DC type 2 (cDC2: *FCER1A*, *CD1C*, *CLEC10A*) (Fig. 2A, Suppl. Fig. 4A). cDC1, but not cDC2, have been previously described in rodent nerves (*13*).The less abundant T/NK cell clusters formed a continuum ranging from CD4 T cell phenotypes, including naive CD4 (*IL7R, CCR7*, *MAL*, *SELL*), Treg (*FOXP3*, *IL2RA*), MAIT (*KLRB1*, *CXCR6*) to CD8 T Cells (*CD8A, CCL5)* and NK cells (*FCGR3A*, *NKG7*, *NCR1*) (Fig. 2A, Suppl. Fig. 4A). Smaller clusters of nuclei represented naive B cells (*CD19*, *MS4A1/*CD20, *CD79B,*) and plasma cells (*JCHAIN*, *SDC1*/CD138) (Fig. 2A, Suppl. Fig. 4A) with mainly *IGHG1*, *IGHG3*, *IGHG4*, and *IGHA1* heavy chain gene expression (Fig. 2E). Granulocytes (*S100A8*, *S100A9*) and mast cells (*CPA3*, *TPSAB1*, *MS4A2*) (Fig. 2A, Suppl. Fig. 4A) were also detected. We thus delineated known and unknown nerve-associated leukocytes in humans in unprecedented detail.

Diverse nerve-associated cell types respond to polyneuropathy.

Having characterized human nerve-associated cells in health, we next aimed to understand how PNP affected the transcriptome and the cellular organization of peripheral nerves. We found that most cell types were present in all human donors, although some patients showed a

grossly skewed composition (Suppl. Fig. 1E). When comparing PNP and CTRL, the most apparent change in PNP was a loss of mySC and the occurrence of damageSC and repairSC (Fig. 3A), known to be induced by nerve damage in rodents(*15*, *23–25*). Additionally, PNP induced an increase in leukocyte clusters; especially Macro1 and Granulo (Fig. 3A). Among IC subclusters, an increase in the endoneurial lipid-associated Macro18 subcluster was the most abundant change in PNP patients (Fig. 3A). Overall, several cell clusters normally predicted to be located within the endoneurium (mySC, endoC) were less abundant, while periC3 increased in PNP (Fig. 3A). This indicated loss of cells located within the endoneurium as a shared feature of human PNPs.

When testing which *individual* single nuclei were associated with disease, the PNP status positively correlated with nuclei in the leukocyte and repairSC clusters and negatively correlated with the mySC cluster after correcting for confounders (Methods) (Fig. 3B, left panel). This means that mySC are less likely to be present in PNP patients on a per nucleus level. In addition, the periC3 cluster positively correlated with PNP disease status (Fig. 3B, left panel). These clusters similarly correlated with clinical disease severity as quantified by the clinical INCAT score (Fig. 3B, middle panel) and myelin thickness (inversely measured by g-ratio) (Fig. 3B, right panel). PNPs thus induced strong compositional changes that also reflected disease severity and affected perineurial cell types.

We then characterized which and how nerve cells *transcriptionally* responded to disease. The number of differentially expressed genes (DEG) was highest in vascular clusters (ven_capEC1, PC2, artEC) followed by endoneurial fibroblasts (endoC) (Fig. 3C). Using a clustering-independent cellular neighborhood-based approach, we accordingly found that cellular neighborhoods with the highest number of DEG were mostly located in vascular clusters (PC2, ven_capEC1, artEC) and in the Macro2 cluster (Fig. 3D). Next, we more

specifically tested how PNP influenced gene expression of selected nerve-associated cells (mySC, nmSC, repairSC, PC2) (Fig. 3E). We found that many of the DEG in the mySC cluster were associated with fibrotic tissue remodeling (e.g., *DCN, TNXB*), extracellular matrix formation (e.g., *COL1A1, COL15A1*), and immune regulation (e.g., *CD53, IL4R, CD74*). The nmSC cluster exhibited transcripts associated with immunosuppression and -modulation (*IL10RA, IL13RA1, CSF2RA, TGFBI*), and the repairSC cluster expressed genes for nerve repair and neuronal differentiation (*GALR1, TMEM47*) (Fig. 3E; Suppl. Tab. 9). GO term enrichment analysis showed that upregulated genes were associated with cell differentiation in the mySC cluster and with cell migration in the nmSC cluster (Suppl. Fig 4B). In the PC2 cell cluster (pericytes), DEG indicated upregulation of molecules related to vessel maintenance (*MFAP5*) and cell adhesion (*NLGN4Y, PCDH11Y),* while genes indicating an interferon-induced immune response (e.g., *IFIT3, OASL, MX1*) were downregulated (Fig. 3E). Consequently, downregulated genes were enriched for antiviral response GO terms (Suppl. Fig. 4B). In summary, PNPs induced transcriptional changes in Schwann cells but also widely outside of the endoneurium, especially in non-endoneurial vascular cells. This suggests that PNPs widely affect the cellular micro-milieu of peripheral nerves and may thus constitute 'pan-nerve diseases'.

PNP subtypes preferentially affect different cellular compartments of peripheral nerves. The etiology of PNP is complex, multiple underlying conditions can lead to PNPs, and the heterogeneity of PNP mechanisms is poorly defined. We therefore next sought to identify cellular or transcriptional patterns specific to individual PNP subtypes. We first classified the available PNP patients by integrating all diagnostic information (Suppl. Tab. 1) into seven subtypes of PNPs: vasculitic (VN, n = 5), chronic inflammatory demyelinating (CIDP, n = 9),

chronic idiopathic axonal (CIAP, n = 11), cancer-associated paraproteinemic (PPN, n = 2), diabetic (DPN, n = 2), other inflammatory (OIN, n = 2), and other non-inflammatory (ONIN, n = 2) (Fig. 4A). We characterized nerves histologically (Methods; Suppl. Fig. 5A). Myelin thickness (inversely quantified by the g-ratio) (Suppl. Fig. 5B-C) and the average number of intactly myelinated axons (Suppl. Fig. 5D) decreased in PNPs, while axon diameter was less affected (Suppl. Fig. 5E). Histological findings in PNP subtypes were in accordance with expectations and also correlated with electrophysiological measures (Suppl. Fig. 5F).

When analyzing the cellular composition determined by snRNA-seq, CTRL samples had the highest relative proportions of the mySC cluster and a low proportion of the repairSC cluster (Fig. 4A). Across conditions, the number of intactly myelinated axons positively correlated with cluster proportions of mySC and negatively correlated with repairSC (Suppl. Fig. 5G). We next compared cluster proportions between groups with at least four samples per group (VN, CIDP, CIAP, CTRL), while disregarding other diagnostic groups due to their small size. In direct comparison with controls, a relative increase in damageSC and repairSC, and loss of mySC was detected in VN, CIDP, CIAP (Fig. 4B). A gain of the periC3 cluster (perineurial cells) and the venEC cluster was shared between VN and CIDP. An increase in the VSMC cluster was found in both VN and CIAP. Loss of the LEC cluster was specific to VN (Fig. 4B). We next compared immune cell sub-cluster proportions between the groups. The lipid-associated Macro18 cluster was increased in all three PNP groups compared to CTRL (Fig. 4C). In contrast, only VN showed an expansion of the plasma cluster. Each PNP subtype thus induced a unique pattern of compositional cellular changes in peripheral nerves.

We then analyzed spatial transcriptomics of sural nerves from VN, CIDP, and CIAP patients in comparison to control (n = 2 per group). Predicted repairSC were increased in the endoneurium in VN compared to CTRL (Fig. 4D). Moreover, mySC were considerably less

abundant in VN compared to CTRL (Fig. 4D). Predicted mySC were also less abundant in CIDP and CIAP compared to CTRL although to a lesser extent than in VN (Suppl. Fig. 5H-I). Quantification of the density of selected leukocyte-associated transcripts (*PTPRC*/CD45, *MS4A1*/CD20, *CD3E*) showed that endo- and epineurial B and T cells increased in VN, CIDP and in CIAP compared to CTRL (Fig. 4F, Suppl. Fig. 5J-). Predicted T_NK cells were more abundant in VN and, to a lesser extent, in CIDP and CIAP than in CTRL (Suppl. Fig. 5 L,M). We thus spatially validated loss of mySC and gain of repairSC and leukocytes in PNPs, especially in VN, as observed in snRNA-seq.

We next aimed to spatially validate the increase in the periC3 (perineurial cell) cluster in snRNA-seq. Plotting known (e.g. *CLDN1, SLC2A1, KRT19*) and novel (e.g. *CXCL14,*) perineurial markers, we found that the perineurium consisted of a single cell layer in CTRL samples, but formed 3-5 cell layers in PNP samples which was most pronounced in CIDP and appeared regionalized (Fig. 4E). The perineurium was also structurally less well defined with a more dispersed and heterogeneous appearance in PNP samples (Fig. 4E). Perineurial hyperplasia and fibrotic dispersion thus occur across PNP subtypes, but preferentially in CIDP.

Next, we tested for subtype-specific transcriptional alterations using a clustering independent approach. In VN, most DEG were located in neighborhoods in the PC2 (pericyte) cluster (Fig. 4G) in accordance with vascular-focused inflammation. In CIDP, DEG were also identified in neighborhoods of vascular clusters (ven_capEC1, artEC, PC2) and the Macro2 cluster. In CIAP, DEG were distributed in a more widespread pattern and also involved the nmSC and the periC2 (perineurial cell) clusters (Fig. 4G). In summary, we defined loss of mySC and non-endoneurial transcriptional alterations as shared across PNPs. Each PNP

subtype additionally induced unique compositional and transcriptional responses, for example immune-associated changes in VN and perineurial dispersion in CIDP.

Hypothesis-free PNP patient classification

Finally, we speculated that PNP patients could be classified purely based on parameters obtained from nerve biopsies by snRNA-seq - a striking difference compared to clinical practice. A principal component analysis (PCA) based on relative cluster abundance showed that VN patients were located in close proximity to each other and separated from other patients (Fig. 5A). This separation was mostly driven by vascular clusters (e.g. artEC, PC1) (Fig. 5A). CIDP and CIAP patients exhibited a larger dispersion in PCA space, potentially indicating a more heterogeneous pathogenesis of CIDP and CIAP (Fig. 5A). Integrating histological measures into the PCA analysis did not show evident enrichment of a certain histological feature in the PCA space.(Suppl. Fig. 6A).

We next used the multi-resolution variational inference (MrVI)(*26*) approach to group patients. This deep generative model is specifically designed for sample-sample comparisons on a single cell level (Methods). We found that patients formed five patient clusters (p-cl; Fig. 5B). A 'normal' cluster of patients (p-cl4) included all CTRL samples and featured normal cluster composition, low disability (i.e., low INCAT), a relatively high number of intact axons, normal axon diameters, and thick myelin (i.e., low g-ratio) (Fig. 5B-F, Suppl. Fig. 6B). A patient cluster (p-cl2) described as 'large-axon-loss' exhibited mildly altered snRNA-seq cluster composition, featuring a reduction of the mySC proportion (Fig. 5E), moderate disability, strong reduction in intact axons, and thinly myelinated remaining axons (Fig. 5B,F, Suppl. Fig. 6B). Another patient cluster (p-cl5) showed severe disability, despite many intact axons and intact myelin thickness but reduction of the endoneurial mySC and nmSC clusters

(Fig. 5B,E), and an increase in endoneurial lipid-associated Macro18 proportions (Fig. 5E; Suppl. Fig. 6D), potentially indicating immune-associated disability. A small patient cluster (p-cl1), consisting of VN patients, showed severe disability, small axon diameters, no relevant demyelination, and an increase in plasma cells (Fig. 5B, D,F). One smaller patient cluster (p-cl3) displayed strong reduction of the mySC and nmSC clusters, (Fig. 5E), an increase in the Treg and CD4_CD8 clusters (Fig. 5D), highest disability, largest axons, a reduction in intact axons and strong demyelination (Fig. 5B, E-F; Suppl. Fig. 6B,C). When plotting the mrVI-based patient classificatio' into the cell cluster abundance-driven PCA, the mrVI patient clusters were separated to some extent. The mean of the 'normal' patient cluster (p-cl4) was closest to the mean of the CTRL patients, supporting this classification (Fig. 5G). Single nuclei transcriptomic information of sural nerves alone was thus useful to categorize PNP patients into pathophysiological groups in a non-hypothesis-driven manner.

Discussion

We aimed to exploit the full potential of human nerve biopsies using state-of-the-art techniques. Here, we present a single nuclei transcriptomics atlas of human sural nerves including 365,708 nuclei of 33 PNP patients and four controls integrated with spatial transcriptomics at subcellular resolution. Capitalizing on this first large-scale technology application to human peripheral nerves and a dataset 10-fold larger than previous rodent studies(*8–13*) we dissected the cellular heterogeneity of human peripheral nerves in detail and found unexpected heterogeneity in perineurial cells. Additionally, we disentangled nerve-associated immune cells and found a multitude of macrophage clusters with an endoneurial to epineurial phenotypic gradient and previously undescribed cDC type 2. We also discovered and validated previously undescribed transcriptional markers of perineurial

fibroblasts (*CXCL14*) and myelinating (*MLIP*) and non-myelinating SC (*GRIK3, PRIMA1*), which were partially human-specific. In human PNP, we identified a loss of myelinating SC, the occurrence of damage and repair SC, and a gain of a lipid-associated macrophage population, as shared features of PNPs. In general, PNP exhibited a loss of cells located in the endoneurium. However, transcriptional changes also affected multiple non-endoneurial cell populations. Thus, PNPs may constitute 'pan-nerve diseases'. Notably, multiple PNPs, especially CIDP, showed perineurial hyperplasia and dispersion. Using single cell transcriptomics to classify PNP patients, we defined patient clusters with specific clinical, histological and cellular phenotypes beyond existing clinical classification. Overall, this suggests a potential of single cell technologies for the classification of PNPs in the future.

Among the novel Schwann cell markers, the *MLIP* gene encodes a muscular laminin-interacting protein, which is required to maintain muscular integrity(*27*) and could serve similar functions in SC. The *PRIMA1*-encoded protein organizes esterases at the neuromuscular junction in terminal SC(*28*), but has not been described in nmSC. *GRIK3* encodes a glutamate ionotropic receptor(*29*) and variants in GRIK3 have been associated with CMT type C(*30*).These genes may thus be involved in structural organization of SC in human peripheral nerves. We additionally identified novel markers for perineurial cells.Human CXCL14 (synonymously BRAK) is constitutively expressed by epithelial tissues and regulates microglial development in the brain(*31*) and neurovascular patterning in the eye(*32*). It is thus conceivable that the perineurium, regarded as an epithelial barrier(*33*), expresses *CXCL14*. The species specificity of some of the markers (*GRIK3, PRIMA1, CXCL14*) could be due to i) size or phylogeny of the mammal, ii) diseased samples, which dominated our dataset, or iii) the purely sensory sural nerve analyzed in humans. We find

differences unlikely to be caused by discrepancies between single nuclei vs. single cell methods because one rodent study analyzed nuclei (*9*) and markers were also not identified.

As a common denominator between the different entities of neuropathies, we observed a relative loss of cells located within the endoneurium. Whether this reflects true cellular loss (i.e. shrinkage) of the endoneurium or cellular transdifferentiation or epi-/perineurial cell proliferation remains to be determined. It is conceivable that loss of myelin-capable axons could be associated with a reduction of SC and other cells located within the endoneurium. Alternatively, a quantitative increase in perineurial cells (e.g. proliferation of the periC3 cluster) could reduce the relative ratio of peri- to endoneurial cells and thereby simulate a *relative* loss of cells with endoneurial location. The perineurium is a lamellated structure made up of concentric cell layers bordered on each side by a basement membrane(*34*). A linear relationship has been described between fascicle diameter and perineurium thickness(*35*), i.e. larger fascicles have a thicker perineurium. Additionally, distal sections have a greater perineurium thickness than proximal segments(*35*). Thickening of the perineurial basement membrane is a characteristic of diabetic PNP(*36*). Focal or generalized perineurial thickening has also been reported in the rare condition 'perineuritis' that can occur either primary or secondary to inflammatory diseases(*37*).Perineurial accumulation of immune cells has also been demonstrated in the early stages of inflammation in a rodent model of autoimmune neuropathy(*38*). The transcription factor *FOXD1*, which was expressed in PNP samples, fate-labels myofibroblast precursors, which contribute to rodent perineurial fibroblasts(*39*) and might play a role in tissue fibrosis(*40*). Overall, perineurial thickening *per se* has not been studied systematically in PNPs and - to our knowledge - the perineurial

distortion described here has not been reported previously. This could reflect a maladaptive response of the nerve microstructure to chronic damage in diverse PNPs.

Diagnosing polyneuropathies can be challenging due to the diverse range of possible causes and the many cases, in which the etiology remains unclear (20-30%)(*5*). Even histology of the sural nerves often fails to establish the etiology of PNP(*7*). Here, we used data-driven approaches to classify patients solely based on snRNA-seq into pathophysiological groups with distinct clinical phenotypes. Therefore, we hypothesize that snRNA-seq could represent a PNP classification tool towards personalized single cell-based neurology/neuro-pathology(*41–43*). This underlines the known heterogeneity in the course and treatment response of neuropathies and suggests that the cellular architecture of the nerve should be taken into account in future studies.

Our study has limitations: Our patient cohort is potentially confounded by immunosuppressive therapy in some patients (Suppl. Tab. 1) and it is unbalanced regarding disease duration, sex and center of origin. However, we provide a large human dataset for single cell/nuclei study standards (37 biological replicates, 365,708 nuclei). Yet, even larger multi-centric multi-national funding, collection and analysis efforts will be required in the future to bring a proposed PNP classification tool to the bedside. Sural nerve biopsies are invasive procedures with some inherent procedural risk and are usually performed in PNP patients which are difficult to diagnose or show rapid disease progression(*7*). Our patient cohort is thus biased towards less frequent PNP etiologies and for example includes only two diabetic PNP, which is the most common cause of PNPs(*1*, *4*, *6*). Furthermore, our analysis is biased towards difficult to diagnose rare cases (e.g. T cell large granular lymphocyte

leukemia associated PNP, S02). We mitigate this by focussing on groups with at least 4 patients. We believe that novel techniques to enrich rare cell types from complex tissue(*44*) could identify PNP-associated cellular patterns in more readily available tissues (e.g. skin biopsies) in the future. Whether less expensive and less labor-intensive methods, such as bulk transcriptomic or methylome analysis of peripheral nerves, could similarly be used for PNP classification remains to be determined. In summary, we provide novel findings regarding the cellular and anatomical architecture of peripheral nerves and define a perspective for developing intra- and inter-PNP classifiers based on single cell technologies towards personalized PNP diagnosis.

References

1. R. Hanewinckel, J. Drenthen, M. van Oijen, A. Hofman, P. A. van Doorn, M. A. Ikram, Prevalence of polyneuropathy in the general middle-aged and elderly population. *Neurology*. **87**, 1892–1898 (2016).
2. E. M. Hoffman, N. P. Staff, J. M. Robb, J. L. St Sauver, P. J. Dyck, C. J. Klein, Impairments and comorbidities of polyneuropathy revealed by population-based analyses. *Neurology*. **84**, 1644–1651 (2015).
3. P. Jennum, R. Ibsen, J. Kjellberg, Health, social and economic consequences of polyneuropathy: a controlled national study evaluating societal effects on patients and their partners. *Eur. Neurol.* **73**, 81–88 (2015).
4. N. A. Visser, N. C. Notermans, R. S. N. Linssen, L. H. van den Berg, A. F. J. E. Vrancken, Incidence of polyneuropathy in Utrecht, the Netherlands. *Neurology*. **84**, 259–264 (2015).
5. R. Hanewinckel, M. van Oijen, M. A. Ikram, P. A. van Doorn, The epidemiology and risk factors of chronic polyneuropathy. *Eur. J. Epidemiol.* **31**, 5–20 (2016).
6. J. Verghese, P. L. Bieri, C. Gellido, H. H. Schaumburg, S. Herskovitz, Peripheral neuropathy in young-old and old-old patients. *Muscle Nerve*. **24**, 1476–1481 (2001).
7. V. Prada, S. Massucco, C. Venturi, A. Geroldi, E. Bellone, P. Mandich, M. Minuto, E. Varaldo, G. Mancardi, M. Grandis, A. Schenone, Diagnostic value of sural nerve biopsy: retrospective analysis of clinical cases from 1981 to 2017. *Front. Neurol.* **10**, 1218 (2019).

8. J. Wolbert, X. Li, M. Heming, A. K. Mausberg, D. Akkermann, C. Frydrychowicz, R. Fledrich, L. Groeneweg, C. Schulz, M. Stettner, N. Alonso Gonzalez, H. Wiendl, R. Stassart, G. Meyer Zu Hörste, Redefining the heterogeneity of peripheral nerve cells in health and autoimmunity. *Proc Natl Acad Sci USA*. **117**, 9466–9476 (2020).

9. A. K. Y. Yim, P. L. Wang, J. R. Bermingham, A. Hackett, A. Strickland, T. M. Miller, C. Ly, R. D. Mitra, J. Milbrandt, Disentangling glial diversity in peripheral nerves at single-nuclei resolution. *Nat. Neurosci.* **25**, 238–251 (2022).

10. D. Gerber, J. A. Pereira, J. Gerber, G. Tan, S. Dimitrieva, E. Yángüez, U. Suter, Transcriptional profiling of mouse peripheral nerves to the single-cell level to build a sciatic nerve ATlas (SNAT). *eLife*. **10** (2021), doi:10.7554/eLife.58591.

11. M. J. Carr, J. S. Toma, A. P. W. Johnston, P. E. Steadman, S. A. Yuzwa, N. Mahmud, P. W. Frankland, D. R. Kaplan, F. D. Miller, Mesenchymal precursor cells in adult nerves contribute to mammalian tissue repair and regeneration. *Cell Stem Cell*. **24**, 240-256.e9 (2019).

12. J. S. Toma, K. Karamboulas, M. J. Carr, A. Kolaj, S. A. Yuzwa, N. Mahmud, M. A. Storer, D. R. Kaplan, F. D. Miller, Peripheral Nerve Single-Cell Analysis Identifies Mesenchymal Ligands that Promote Axonal Growth. *eNeuro*. **7** (2020), doi:10.1523/ENEURO.0066-20.2020.

13. D. Lovatt, A. Tamburino, A. Krasowska-Zoladek, R. Sanoja, L. Li, V. Peterson, X. Wang, J. Uslaner, scRNA-seq generates a molecular map of emerging cell subtypes after sciatic nerve injury in rats. *Commun. Biol.* **5**, 1105 (2022).

14. F. J. Garcia, N. Sun, H. Lee, B. Godlewski, H. Mathys, K. Galani, B. Zhou, X. Jiang, A. P. Ng, J. Mantero, L.-H. Tsai, D. A. Bennett, M. Sahin, M. Kellis, M. Heiman, Single-cell dissection of the human brain vasculature. *Nature*. **603**, 893–899 (2022).

15. P. J. Arthur-Farraj, C. C. Morgan, M. Adamowicz, J. A. Gomez-Sanchez, S. V. Fazal, A. Beucher, B. Razzaghi, R. Mirsky, K. R. Jessen, T. J. Aitman, Changes in the Coding and Non-coding Transcriptome and DNA Methylome that Define the Schwann Cell Repair Phenotype after Nerve Injury. *Cell Rep.* **20**, 2719–2734 (2017).

16. S. P. Palladino, E. S. Helton, P. Jain, C. Dong, M. R. Crowley, D. K. Crossman, E. E. Ubogu, The Human Blood-Nerve Barrier Transcriptome. *Sci. Rep.* **7**, 17477 (2017).

17. C. A. P. Wood, J. Zhang, D. Aydin, Y. Xu, B. J. Andreone, U. H. Langen, R. O. Dror, C. Gu, L. Feng, Structure and mechanism of blood-brain-barrier lipid transporter MFSD2A. *Nature*. **596**, 444–448 (2021).

18. A. Janesick, R. Shelansky, A. D. Gottscho, F. Wagner, S. R. Williams, M. Rouault, G. Beliakoff, C. A. Morrison, M. F. Oliveira, J. T. Sicherman, A. Kohlway, J. Abousoud, T. Y. Drennon, S. H. Mohabbat, 10x Development Teams, S. E. B. Taylor, High resolution mapping of the tumor microenvironment using integrated single-cell, spatial and in situ analysis. *Nat. Commun.* **14**, 8353 (2023).

19. B. Chen, M. C. Banton, L. Singh, D. B. Parkinson, X.-P. Dun, Single cell transcriptome data analysis defines the heterogeneity of peripheral nerve cells in homeostasis and regeneration. *Front. Cell. Neurosci.* **15**, 624826 (2021).

20. A. L. Kalinski, C. Yoon, L. D. Huffman, P. C. Duncker, R. Kohen, R. Passino, H. Hafner, C. Johnson, R. Kawaguchi, K. S. Carbajal, J. S. Jara, E. Hollis, D. H. Geschwind, B. M. Segal, R. J. Giger, Analysis of the immune response to sciatic nerve injury identifies efferocytosis as a key mechanism of nerve debridement. *eLife*. **9** (2020), doi:10.7554/eLife.60223.

21. E. Ydens, L. Amann, B. Asselbergh, C. L. Scott, L. Martens, D. Sichien, O. Mossad, T. Blank, S. De Prijck, D. Low, T. Masuda, Y. Saeys, V. Timmerman, R. Stumm, F. Ginhoux, M. Prinz, S. Janssens, M. Guilliams, Profiling peripheral nerve macrophages reveals two macrophage subsets with distinct localization, transcriptome and response to injury. *Nat. Neurosci.* **23**, 676–689 (2020).

22. P. L. Wang, A. K. Y. Yim, K.-W. Kim, D. Avey, R. S. Czepielewski, M. Colonna, J. Milbrandt, G. J. Randolph, Peripheral nerve resident macrophages share tissue-specific programming and features of activated microglia. *Nat. Commun.* **11**, 2552 (2020).

23. J. A. Gomez-Sanchez, K. S. Pilch, M. van der Lans, S. V. Fazal, C. Benito, L. J. Wagstaff, R. Mirsky, K. R. Jessen, After nerve injury, lineage tracing shows that myelin and remak schwann cells elongate extensively and branch to form repair schwann cells, which shorten radically on remyelination. *J. Neurosci.* **37**, 9086–9099 (2017).

24. C. Norrmén, G. Figlia, P. Pfistner, J. A. Pereira, S. Bachofner, U. Suter, mTORC1 Is Transiently Reactivated in Injured Nerves to Promote c-Jun Elevation and Schwann Cell Dedifferentiation. *J. Neurosci.* **38**, 4811–4828 (2018).

25. F. Szepanowski, M. Winkelhausen, R. D. Steubing, A. K. Mausberg, C. Kleinschnitz, M. Stettner, LPA1 signaling drives Schwann cell dedifferentiation in experimental autoimmune neuritis. *J. Neuroinflammation*. **18**, 293 (2021).

26. P. Boyeau, J. Hong, A. Gayoso, M. Jordan, E. Azizi, N. Yosef, Deep generative modeling for quantifying sample-level heterogeneity in single-cell omics. *BioRxiv* (2022), doi:10.1101/2022.10.04.510898.

27. M.-E. Cattin, S. A. Deeke, S. A. Dick, Z. J. A. Verret-Borsos, G. Tennakoon, R. Gupta, E. Mak, C. L. Roeske, J. J. Weldrick, L. A. Megeney, P. G. Burgon, Expression of murine muscle-enriched A-type lamin-interacting protein (MLIP) is regulated by tissue-specific alternative transcription start sites. *J. Biol. Chem.* **293**, 19761–19770 (2018).

28. K. A. Petrov, E. Girard, A. D. Nikitashina, C. Colasante, V. Bernard, L. Nurullin, J. Leroy, D. Samigullin, O. Colak, E. Nikolsky, B. Plaud, E. Krejci, Schwann cells sense and control acetylcholine spillover at the neuromuscular junction by α7 nicotinic

receptors and butyrylcholinesterase. *J. Neurosci.* **34**, 11870–11883 (2014).

29. N. Strutz, C. Villmann, A. Thalhammer, P. Kizelsztein, M. Eisenstein, V. I. Teichberg, M. Hollmann, Identification of domains and amino acids involved in GLuR7 ion channel function. *J. Neurosci.* **21**, 401–411 (2001).

30. M. Vedi, J. R. Smith, G. Thomas Hayman, M. Tutaj, K. C. Brodie, J. L. De Pons, W. M. Demos, A. C. Gibson, M. L. Kaldunski, L. Lamers, S. J. F. Laulederkind, J. Thota, K. Thorat, M. A. Tutaj, S.-J. Wang, S. Zacher, M. R. Dwinell, A. E. Kwitek, 2022 updates to the Rat Genome Database: a Findable, Accessible, Interoperable, and Reusable (FAIR) resource. *Genetics*. **224** (2023), doi:10.1093/genetics/iyad042.

31. Z. Li, Y. Li, J. Jiao, Neural progenitor cells mediated by H2A.Z.2 regulate microglial development via Cxcl14 in the embryonic brain. *Proc Natl Acad Sci USA*. **116**, 24122–24132 (2019).

32. A. F. Ojeda, R. P. Munjaal, P. Y. Lwigale, Knockdown of CXCL14 disrupts neurovascular patterning during ocular development. *Dev. Biol.* **423**, 77–91 (2017).

33. E. E. Ubogu, Biology of the human blood-nerve barrier in health and disease. *Exp. Neurol.* **328**, 113272 (2020).

34. R. E. Hill, R. E. Williams, A quantitative analysis of perineurial cell basement membrane collagen IV, laminin and fibronectin in diabetic and non-diabetic human sural nerve. *J. Anat.* **201**, 185–192 (2002).

35. F. R. Andreis, B. Metcalfe, T. Al Muhammadee Janjua, V. P. S. Fazan, W. Jensen, S. Meijs, T. G. N. dos Santos Nielsen, in *2023 11th International IEEE/EMBS Conference on Neural Engineering (NER)* (IEEE, 2023), pp. 1–4.

36. R. E. Hill, P. E. Williams, Perineurial cell basement membrane thickening and myelinated nerve fibre loss in diabetic and nondiabetic peripheral nerve. *J. Neurol. Sci.* **217**, 157–163 (2004).

37. M. P. Collins, R. D. M. Hadden, N. Shahnoor, Primary perineuritis, a rare but treatable neuropathy: Review of perineurial anatomy, clinicopathological features, and differential diagnosis. *Muscle Nerve*. **68**, 696–713 (2023).

38. A. K. Mausberg, F. Szepanowski, F. Odoardi, A. Flügel, C. Kleinschnitz, M. Stettner, B. C. Kieseier, Trapped in the epineurium: early entry into the endoneurium is restricted to neuritogenic T cells in experimental autoimmune neuritis. *J. Neuroinflammation*. **15**, 217 (2018).

39. G. Nikoloudaki, D. W. Hamilton, Assessing the fate and contribution of Foxd1-expressing embryonic precursors and their progeny in palatal development, homeostasis and excisional repair. *Sci. Rep.* **14**, 4969 (2024).

40. A. K. Ajay, L. Zhao, S. Vig, M. Fujiwara, S. Thakurela, S. Jadhav, A. Cho, I.-J. Chiu, Y. Ding, K. Ramachandran, A. Mithal, A. Bhatt, P. Chaluvadi, M. K. Gupta, S. I. Shah,

V. S. Sabbisetti, A. M. Waaga-Gasser, D. A. Frank, G. Murugaiyan, J. V. Bonventre, L.-L. Hsiao, Deletion of STAT3 from Foxd1 cell population protects mice from kidney fibrosis by inhibiting pericytes trans-differentiation and migration. *Cell Rep.* **38**, 110473 (2022).

41. J. Lim, V. Chin, K. Fairfax, C. Moutinho, D. Suan, H. Ji, J. E. Powell, Transitioning single-cell genomics into the clinic. *Nat. Rev. Genet.* **24**, 573–584 (2023).

42. M. Heming, A.-L. Börsch, H. Wiendl, G. Meyer Zu Hörste, High-dimensional investigation of the cerebrospinal fluid to explore and monitor CNS immune responses. *Genome Med.* **14**, 94 (2022).

43. G. Meyer Zu Hörste, C. C. Gross, L. Klotz, N. Schwab, H. Wiendl, Next-Generation Neuroimmunology: New Technologies to Understand Central Nervous System Autoimmunity. *Trends Immunol.* **41**, 341–354 (2020).

44. I. C. Clark, M. A. Wheeler, H.-G. Lee, Z. Li, L. M. Sanmarco, S. Thaploo, C. M. Polonio, S. W. Shin, G. Scalisi, A. R. Henry, J. M. Rone, F. Giovannoni, M. Charabati, C. F. Akl, D. M. Aleman, S. E. J. Zandee, A. Prat, D. C. Douek, E. A. Boritz, F. J. Quintana, A. R. Abate, Identification of astrocyte regulators by nucleic acid cytometry. *Nature*. **614**, 326–333 (2023).

45. P. Y. K. Van den Bergh, P. A. van Doorn, R. D. M. Hadden, B. Avau, P. Vankrunkelsven, J. A. Allen, S. Attarian, P. H. Blomkwist-Markens, D. R. Cornblath, F. Eftimov, H. S. Goedee, T. Harbo, S. Kuwabara, R. A. Lewis, M. P. Lunn, E. Nobile-Orazio, L. Querol, Y. A. Rajabally, C. Sommer, H. A. Topaloglu, European Academy of Neurology/Peripheral Nerve Society guideline on diagnosis and treatment of chronic inflammatory demyelinating polyradiculoneuropathy: Report of a joint Task Force-Second revision. *Eur. J. Neurol.* **28**, 3556–3583 (2021).

46. A.-H. Pool, H. Poldsam, S. Chen, M. Thomson, Y. Oka, Recovery of missing single-cell RNA-sequencing data with optimized transcriptomic references. *Nat. Methods*. **20**, 1506–1515 (2023).

47. S. J. Fleming, M. D. Chaffin, A. Arduini, A.-D. Akkad, E. Banks, J. C. Marioni, A. A. Philippakis, P. T. Ellinor, M. Babadi, Unsupervised removal of systematic background noise from droplet-based single-cell experiments using CellBender. *Nat. Methods*. **20**, 1323–1335 (2023).

48. Y. Hao, T. Stuart, M. H. Kowalski, S. Choudhary, P. Hoffman, A. Hartman, A. Srivastava, G. Molla, S. Madad, C. Fernandez-Granda, R. Satija, Dictionary learning for integrative, multimodal and scalable single-cell analysis. *Nat. Biotechnol.* **42**, 293–304 (2024).

49. P.-L. Germain, A. Lun, C. Garcia Meixide, W. Macnair, M. D. Robinson, Doublet identification in single-cell sequencing data using scDblFinder. *F1000Res.* **10**, 979 (2021).

50. R. Lopez, J. Regier, M. B. Cole, M. I. Jordan, N. Yosef, Deep generative modeling for single-cell transcriptomics. *Nat. Methods*. **15**, 1053–1058 (2018).

51. M. V. Kuleshov, M. R. Jones, A. D. Rouillard, N. F. Fernandez, Q. Duan, Z. Wang, S. Koplev, S. L. Jenkins, K. M. Jagodnik, A. Lachmann, M. G. McDermott, C. D. Monteiro, G. W. Gundersen, A. Ma'ayan, Enrichr: a comprehensive gene set enrichment analysis web server 2016 update. *Nucleic Acids Res.* **44**, W90-7 (2016).

52. J. W. Squair, M. Gautier, C. Kathe, M. A. Anderson, N. D. James, T. H. Hutson, R. Hudelle, T. Qaiser, K. J. E. Matson, Q. Barraud, A. J. Levine, G. La Manno, M. A. Skinnider, G. Courtine, Confronting false discoveries in single-cell differential expression. *Nat. Commun.* **12**, 5692 (2021).

53. M. D. Robinson, D. J. McCarthy, G. K. Smyth, edgeR: a Bioconductor package for differential expression analysis of digital gene expression data. *Bioinformatics*. **26**, 139–140 (2010).

54. A. Missarova, E. Dann, L. Rosen, R. Satija, J. Marioni, Sensitive cluster-free differential expression testing. *BioRxiv* (2023), doi:10.1101/2023.03.08.531744.

55. B. Phipson, C. B. Sim, E. R. Porrello, A. W. Hewitt, J. Powell, A. Oshlack, propeller: testing for differences in cell type proportions in single cell data. *Bioinformatics*. **38**, 4720–4726 (2022).

56. Y. A. Reshef, L. Rumker, J. B. Kang, A. Nathan, I. Korsunsky, S. Asgari, M. B. Murray, D. B. Moody, S. Raychaudhuri, Co-varying neighborhood analysis identifies cell populations associated with phenotypes of interest from single-cell transcriptomics. *Nat. Biotechnol.* **40**, 355–363 (2022).

57. F. Husson, J. Josse, S. Lê, FactoMineR : An *R* package for multivariate analysis. *J. Stat. Softw.* **25** (2008), doi:10.18637/jss.v025.i01.

58. B. Cakir, M. Prete, N. Huang, S. van Dongen, P. Pir, V. Y. Kiselev, Comparison of visualization tools for single-cell RNAseq data. *NAR Genom. Bioinform.* **2**, lqaa052 (2020).

59. R. Hillje, P. G. Pelicci, L. Luzi, Cerebro: interactive visualization of scRNA-seq data. *Bioinformatics*. **36**, 2311–2313 (2020).

60. N. Pielawski, A. Andersson, C. Avenel, A. Behanova, E. Chelebian, A. Klemm, F. Nysjö, L. Solorzano, C. Wählby, TissUUmaps 3: Improvements in interactive visualization, exploration, and quality assessment of large-scale spatial omics data. *Heliyon*. **9**, e15306 (2023).

Acknowledgements

We are deeply indebted to the patients for their participation. We thank Rebecca Ley from the Institute of Neuropathology Münster for excellent technical histological assistance. We would like to thank Kristina Wagner for the technical assistance with processing of the samples in Essen. This work was supported by the Core EM and Histology, a core facility of the CMCB Technology Platform at the Technische Universität Dresden. We thank Susanne Weiche for excellent technical assistance in preparing the Xenium slides. Part of the calculations were performed on the high performance computing (HPC) cluster PALMA II of the University of Münster, subsidized by the DFG (INST 211/667-1).

Funding

This project was mainly funded by a grant from the Bundesministerium für Bildung und Forschung (BMBF) 'Lipid Immune Neuropathy Consortium' (to G.M.z.H., M.S., R.S., R.F.) and a grant from the Interdisziplinäres Zentrum für Klinische Forschung (IZKF) Münster (SEED/016/21 to M.H.). Additionally, GMzH was supported by grants from the Deutsche Forschungsgemeinschaft (DFG) (ME4050/12-1, ME4050/13-1, ME4050/8-1). This project was also supported by the DFG Sonderforschungsbereich Transregio 128 (to H.W.).

Author contributions

M.H. and G.M.z.H. conceived and supervised the study. M.H., J.T, A.K.M, M.M., M.S., A.-K.U., C.D., K.K., F.S, B.E, K.L., and C.S. were involved in collecting human sural nerves. J.T. performed nuclei extraction and snRNA-seq experiments. I.-N.L. carried out sequencing of snRNA-seq. J.W. planned the Xenium analysis. J.A., A.D. performed Xenium experiments. F.D. determined g-ratios. M.H. and C.S. gathered sample and patient metadata.

M.H. performed computational analyses. C.T., R.S., R.F., H.W., C.S., and M.S. co-supervised the study. A.-L.B. designed the figures and schemes. M.H., J.W. and G.M.z.H. wrote the manuscript. All authors read and approved the manuscript.

Competing interest

M.H., J.W. and G.M.z.H. have submitted a patent application for the diagnostic classification of PNP patients by single nuclei transcriptomics of human nerve material. The remaining authors report no conflict of interest.

Data and code availability

All raw and processed single cell sequencing data with sample and cluster annotations will be publicly available in GEO. An interactive version of the snRNA-seq data, created with cerebroApp v1.4.2(*59*) and an interactive version of the Xenium data, created with TissUUmaps v3.1(*60*), is available at http://pns-atlas.mzhlab.com. The code is publicly available at https://github.com/mihem/pns_atlas.

Supplementary Materials

Materials and Methods

Fig S1 to S6

Tables S1 to S9

References 45 to 60

Figures

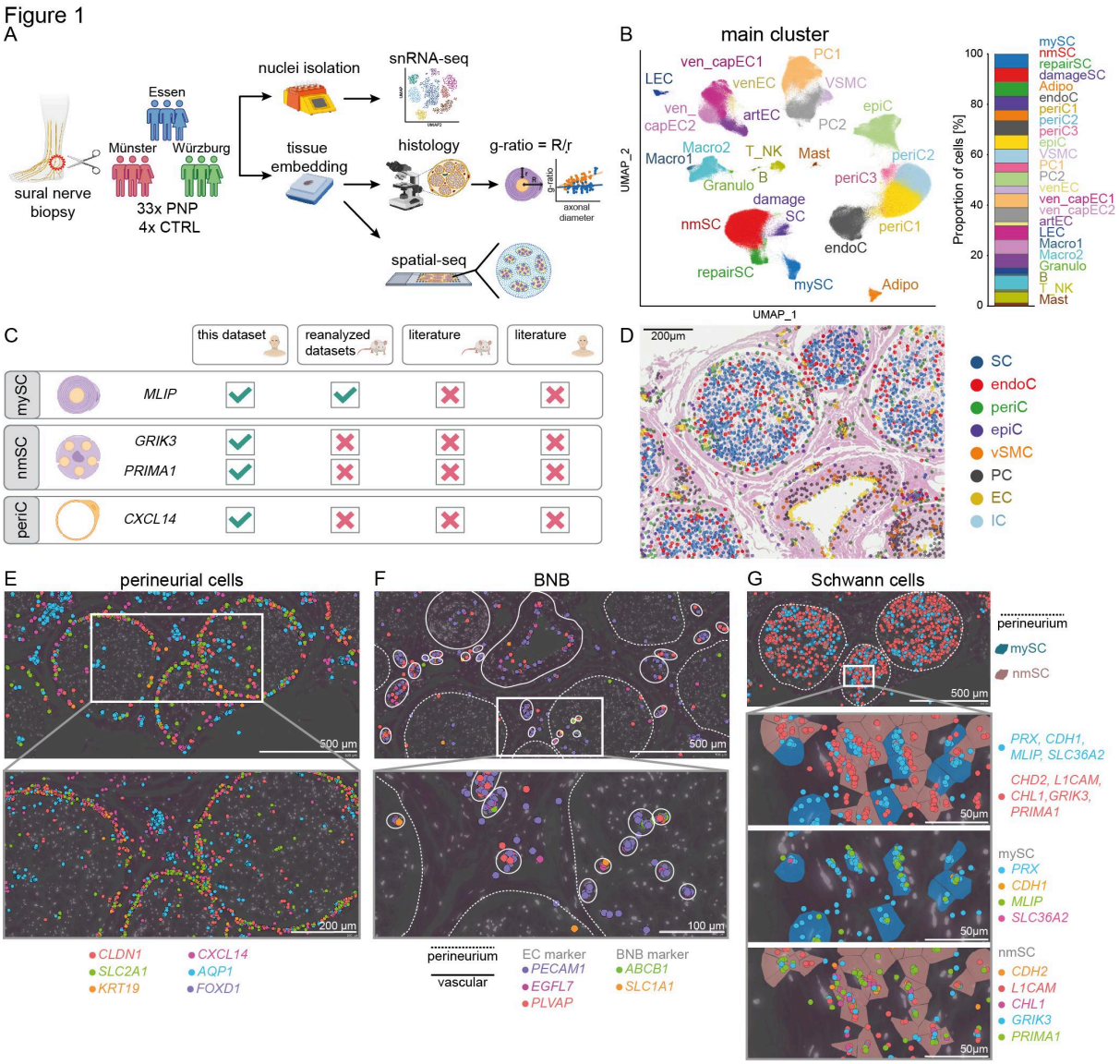

Figure 1: Defining the species-specific cellular landscape of human peripheral nerves

(A) Schematic overview of the experimental procedure. Sural nerve biopsies were collected from 33 polyneuropathy (PNP) patients and four controls (CTRL) from three German centers (Essen, Münster, Würzburg) and processed by single nuclei RNA-sequencing (snRNA-seq). Additionally, subcellular spatial transcriptomics (Xenium) was performed in a subgroup of eight patients. All 37 tissues were histologically characterized by quantifying myelin

thickness (g-ratio), number of intactly myelinated axons and axon diameters. **(B)** UMAP of 365,708 high-quality nuclei from 37 human sural nerves, showing 23 main clusters. **(C)** Schematic depicting if novel marker genes of human myelinating Schwann cells (mySC), non-myelinating Schwann cells (nmSC), and perineurial cells (periC) found in this dataset were detected when reanalyzing published rodent dataset (Yim et al., Gerber et al., Wolbert et al., Supp. Tabl. 4-6) and whether these markers were previously described in rodent or human literature. **(D)** Representative section of an H&E staining overlaid with spatial-seq (Xenium) showing predicted clusters in spatial-seq of a sural nerve cross section of CTRL patient S24. Each dot represents one cell **(E)-(G)** Representative spatial-seq images of selected genes expressed in (E) perineurial cells, (F) in cells of the blood nerve barrier (BNB), and (G) in mySC (blue highlight) and nmSC (red highlight) in the sural nerve of CTRL patient S24. Each dot represents the expression of one transcript, a dotted line marks the perineurium, and a solid line surrounds individual vessels.

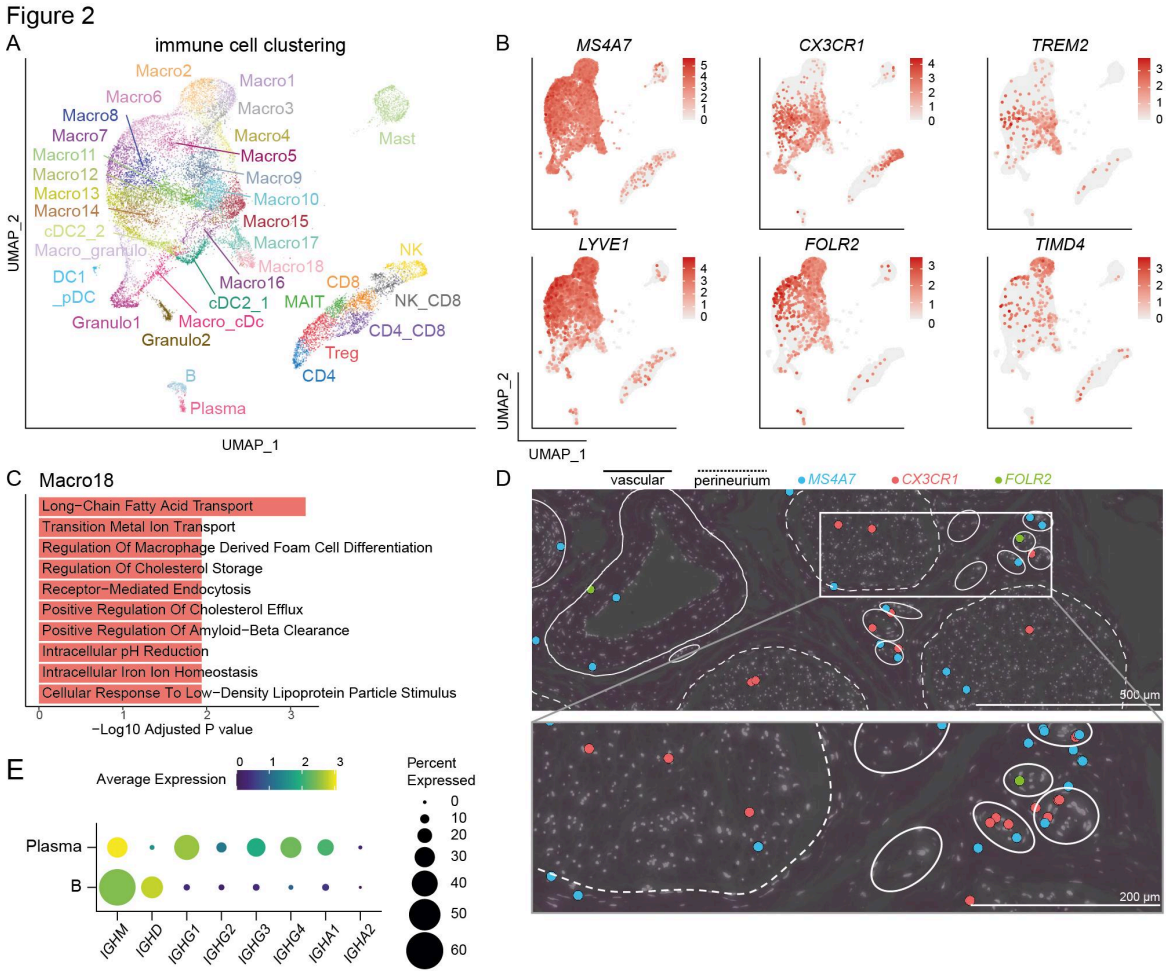

Figure 2: Heterogeneity of human nerve-associated immune cells

(A) UMAP of 18,436 nuclei representing 35 immune cell (IC) subclusters of 37 human sural nerves. **(B)** Feature plots of known endoneurial and epineurial macrophage marker genes. Color encodes gene expression. **(C)** Gene ontology term enrichment analysis of marker genes ($\log_2$ fold change > 2, adjusted p value < 0.001) expressed by the Macro18 IC cluster in a one vs. all IC cluster comparison. **(D)** Representative spatial-seq images of the macrophage marker *MS4A7* and the endoneurial macrophage markers *CX3CR1* and *TREM2* in the sural nerve of CTRL patient S24. Each dot represents the expression of one transcript, a dotted line marks the perineurium, and a solid line surrounds individual vessels. **(E)** Expression of immunoglobulin heavy (*IGH*) chain genes in the B cell (B) and plasma cell (plasma) cluster

of the IC subclusters. Dot size encodes the percentage of cells expressing the transcript, and color shows the average gene expression.

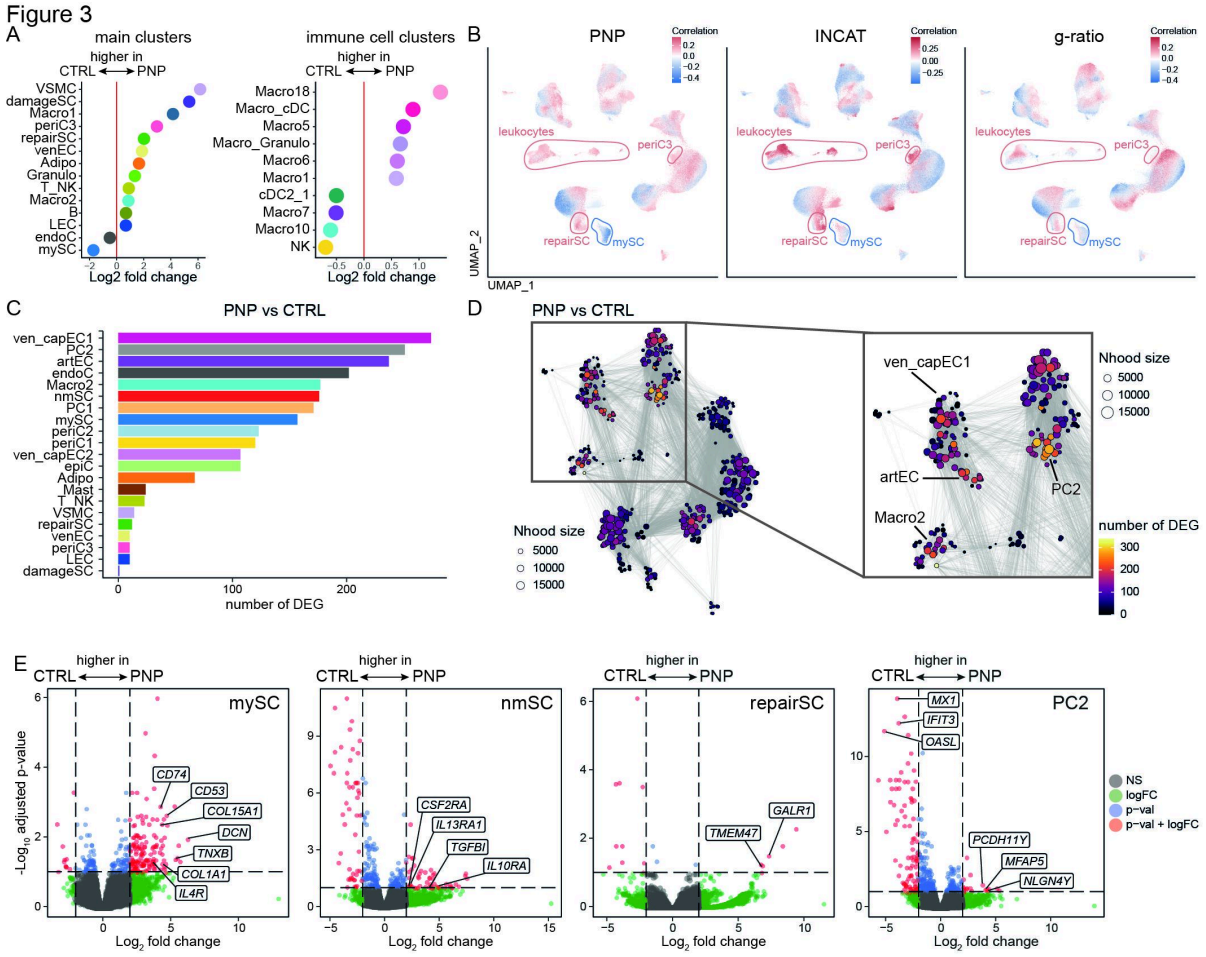

Figure 3: Identifying a pan-neuropathy cellular transcriptional response pattern

(A) Differences in cluster abundance in patients with polyneuropathy (PNP) vs. controls (CTRL), left: main clusters (Fig. 1B), right: immune cell subclusters (Fig.2A). Only clusters with a $\log_2$ fold change > 0.5 are shown. **(B)** Correlations between individual single nuclei and PNP status (right), clinical Inflammatory Neuropathy Cause and Treatment (INCAT) disability score (middle), and g-ratio of myelinated axons (right) are shown. Red indicates a positive correlation and blue a negative correlation. **(C)** The number of differentially expressed genes (DEG) per cell cluster were determined in a pseudo bulk approach and are

visualized. **(D)** Neighborhood graph displaying the number of DEG between PNP and CTRL in a clustering-independent cellular neighborhood-based approach. Each dot represents a neighborhood, and the dot size represents the size of the neighborhood (Nhood), while edges depict the number of cells shared between neighborhoods. Color code shows the number of DEG. The right plot shows a magnification of the left plot, highlighting neighborhoods/clusters with the highest number of DEG. **(E)** Volcano plots of DEG in myelinating Schwann cells (mySC), non-myelinating SC (nmSC), repair SC, and pericytes 2 (PC2) between PNP and CTRL. The horizontal dashed line represents an adjusted p value of 0.1 and the vertical dashed lines display a $\log_2$ fold change of 2 Selected transcripts above those thresholds are labeled.

Figure 4

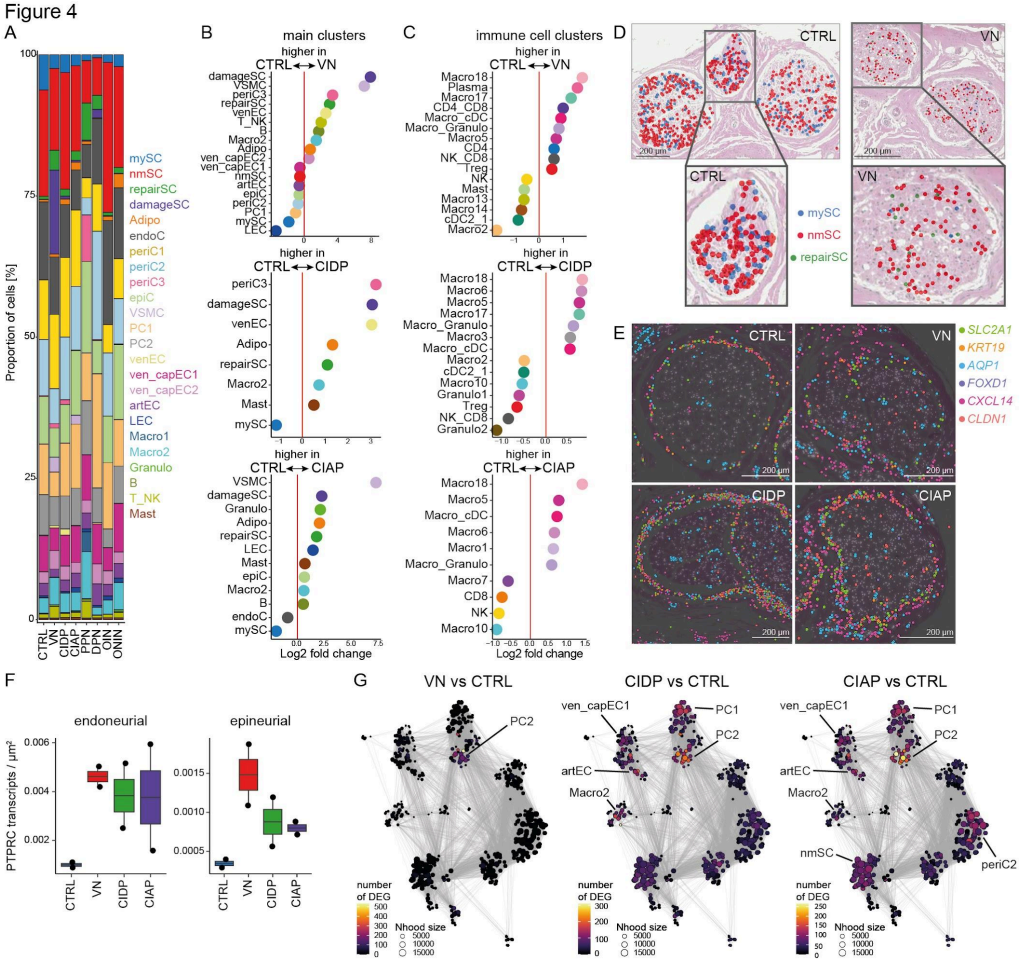

Figure 4: PNP subtypes affect different cellular compartments of peripheral nerves

(A) Proportion of cells split by disease group and colored by the main clusters. **(B) - (C)** Changes of cluster abundance in patients with vasculitic (VN), chronic inflammatory demyelinating (CIDP), and chronic idiopathic axonal (CIAP) polyneuropathy vs. controls (CTRL). The left plots show changes of the main clusters (as in Fig. 1B), the left plots show differences in the immune cell subclusters (Fig. 2A).Only clusters with a $\log_2$ fold change > 0.5 are shown. **(D)** Representative sections of H&E staining of sural nerves overlaid with spatial seq (Xenium) showing predicted Schwann cell clusters in CTRL (S24, left plot), and VN (S30, right plot) patients. Each dot represents one cell. **(E)** Representative spatial transcriptomics images of perineurial marker genes of CTRL (S24), VN (S30), CIDP (S01), and CIAP (S14). Each dot represents the expression of one transcript. **(F)** The density of *PTPRC* transcripts in the endoneurial (left pot) and epineurial (right plot) per disease group (n = 2 per disease group). **(G)** Neighborhood graphs displaying the number of DEG between PNP patients with VN (left), CIDP (middle) or CIAP (right) and CTRL in a clustering-independent cellular neighborhood-based approach. Dot size represents neighborhoods (Nhood), while edges depict the number of cells shared between neighborhoods. Color code shows the number of DEG.

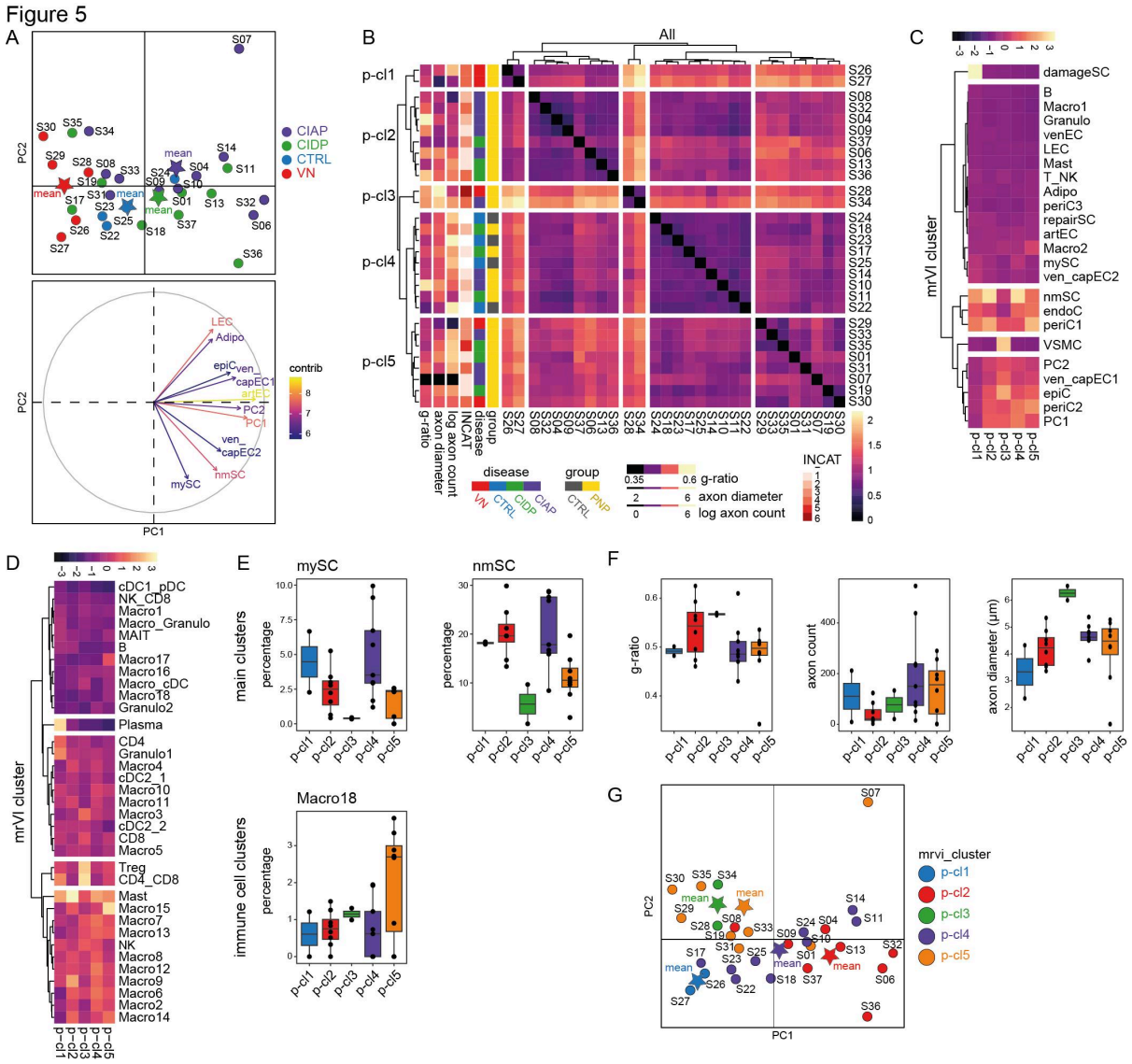

Figure 5: Hypothesis-free PNP patient classification

(A) Upper plot: PCA based on the relative cluster abundance in 29 patients categorized by disease group (vasculitic PNP, VN, n = 5), chronic inflammatory demyelination (CIDP, n = 9), chronic idiopathic axonal (CIAP, n = 11)) and controls (CTRL, n = 4). Each dot represents a patient, the star represents the group mean. Lower plot: Individual variables of the PCA. The contribution of each variable is color-coded. **(B)** Patient-patient comparisons were conducted with a deep generative model (multi-resolution variational inference). Patient-patient distances were visualized in a hierarchically clustered heatmap. The heatmap

is annotated with clinical (group, disease, INCAT disability score) and histological (number of intactly myelinated axons, g-ratio, axon diameter). **(C-D)** Scaled cellular abundance per patient clusters (defined in **B**) of main clusters (**C**) and immune cell subclusters (**D**) visualized in a clustered heatmap. **(E)** Abundance of selected cell clusters per patient clusters. **(F)** Histological measures (g-ratio, number of intactly myelinated axons, axon diameter) per patient cluster. (**G**) PCA based on the relative cluster abundance (as in A), but categorized by patient-clusters.

Materials and Methods

Collection of patient samples

We collected sural nerves from 33 PNP patients from three centers: University Hospital of Münster (10), Essen (11), and Würzburg (12). Additionally, we obtained sural nerves from four control patients in Essen with traumatic nerve injuries, who received a sural nerve autograft as interposition, but were unaffected by polyneuropathy (Suppl. Tab. 1). Residual material from the sural nerve grafts were used for control samples in this study. In PNP patients, sural nerve biopsy was performed as part of the clinical diagnostic workup and a small portion of the nerve (approximately 0.2 cm) was used for this study. In Münster and Essen, the samples were immediately fresh-frozen after surgery in dry ice-cooled methylbutane and stored in liquid nitrogen (0 - 14 months, Suppl. Tab. 1) until nuclei extraction. In Würzburg, the samples were embedded into OCT embedding matrix (Roth) until nuclei extraction (33 - 77 months, Suppl. Tab. 1). In Essen and Münster samples were collected from newly recruited patients. In Würzburg, samples were collected from an existing biobank of OCT embedded cryo-preserved sural nerve biopsies collected between 2016 and 2020. All experiments were carried out in accordance with the Declaration of

Helsinki and were approved by the local ethical committees in Münster (2018-719-f-S), Essen (21-10376-BO), and Würzburg (238/17; 15/19). All patients gave written informed consent to sample collection.

Patient characteristics

Patients were characterized clinically regarding diagnosis, disease activity, therapy response, disease duration, immunosuppressive therapy, relevant secondary diagnosis, electrophysiological studies and CSF analysis outlined in Suppl. Tab. 1. Patients were diagnosed according to the EAN/PNS criteria 2021 for CIDP(*45*) and according to the PNS criteria for VN.

Nuclei extraction and purification

For each patient, approximately 10 mg pieces (median of 13.9 mg) were cut on dry ice as starting material from the original samples. Nerve pieces were cut into smaller pieces and processed using the Miltenyi Biotec nuclei extraction protocol. In summary, samples were transferred to a gentleMACS C-tube (Cat.no. 130-093-237) containing 2 ml lysis buffer (nuclei extraction buffer (Cat. no. 130-128-024) + 0.2 U/µl RNase inhibitor (EO0381) and processed on a gentleMACS dissociator with program 4C_nuclei_1. After dissociation, the nuclei suspension was filtered through a pluriStrainer Mini 70-µm cell strainer (pluriSelect®) and washed in 200-400 µl resuspension buffer (PBS with 0.1% BSA and 0.2 U/µL RNase inhibitor (EO0381) depending on sample size and expected nuclei count. Nuclei suspension was then filtered through a pluriStrainer Mini 40-µm cell strainer (pluriSelect®), placed on a 1.5 ml DNA-LoBind tube (Merck). The nuclei suspension was stained with Trypan Blue to

manually assess nuclei viability and count using a Fuchs-Rosenthal chamber. Equal volumes between samples were used for downstream application single nuclei RNA seq.

Single nuclei RNA-sequencing and generation of count matrices

Single nuclei suspensions were loaded into a Chromium Next GEM Chip G and placed into the Chromium X Single Cell Controller and processed with Chromium Next GEM Single Cell 3′ Kit v3.1 reagents (all 10X Genomics). Sequencing was performed on Illumina Nextseq 2000 and Novaseq 6000 with a 28-8-0-91 read setup. We used cellranger v7.0.1 (10X Genomics) to generate count matrices with default parameters but an optimized transcriptome reference v1.1(*46*) for GRCh38.

Single nuclei analysis

CellBender v0.3.0(*47*) was used to remove background noise. In CellBender, the number of expected cells and total droplets was based on the UMI curve and the learning rate was reduced based on the automated output report. Further downstream analysis was performed with the R package Seurat v5.0.1(*48*). To increase computational efficiency and reduce memory usage of this large dataset, we used BPCells v0.1.0. Low quality cells were filtered for each sample individually by inspecting quality control plots and removing cells with higher mitochondrial percentages (range: 1-5%), low (<200) or very high molecule counts per cell (range: 6000-9000). Doublets were removed using scDblFinder v1.16.0(*49*) with default parameters. We used Seurat for normalization (LogNormalize, default parameters), identification of highly variable genes (vst method,2000 features), scaling, and performing PCA (default parameters). Next, we used atomic sketch integration (method LeverageScore, 5000 cells) in Seurat to reduce memory usage. Batch effects were accounted for by

integrating the samples with scVI v1.0.4(*50*). After inspecting the effect of batch removal, the full dataset was integrated with Seurat. The scVI integrated full dataset was used to calculate the UMAP embeddings with Seurat (30 dimensions). We identified clusters with the FindNeighbors and FindClusters (resolution 0.7) functions. We calculated the top expressing genes of each cluster with FindMarkers (min.pct = 0.1, logfc_threshold = 0.25, p_val_adj < 0.05, two-sided Wilcoxon rank-sum test). To subcluster the immune cells, we selected the immune cell clusters of the main clusters. We then reperformed identification of highly variable genes, scaling, and PCA as explained above. The data were integrated with reciprocal PCA using Seurat and after plausibility checks of the batch removal, UMAP was calculated (30 dimensions). Clusters were identified with FindNeighbors and FindClusters (resolution 2.3). The top expressing genes were identified as explained for the main clusters. Enrichment analysis of top markers (avg_log2FC > 1, p_val_adj < 0.001) was carried out with enrichR 3.2(*51*) with the GO Biological Process 2023 database. Differentially expressed genes between conditions were identified using a pseudobulk method with Libra v1.0.0(*52*) (edgeR 4.0.7(*53*), two-sided likelihood ratio test). Volcano plots of DE genes were created with Enhanced Volcano v1.20.0. Additionally, we determined DE genes in a cluster-independent manner with miloDE v0.0.0.9 (*54*) following the tutorial. Briefly, neighborhoods were assigned based on the scvi integrated data (k = 30, prop = 0.1, d = 30) and DE testing was conducted between conditions (min_count =10). To determine the cluster abundance, we used propeller(*55*) (part of speckle v1.2.0). We used the co-varying neighborhood analysis (CNA), implemented in the rcna package v0.0.99(*56*), to compute correlations between clinical phenotypes or histological measures and our single cell data independent of clustering controlling for age and sex. To classify patients we used the PCA of the cluster abundance and multi-resolution variational interference (MrVI)(*26*). PCA of the

cluster abundances and variable contributions were calculated and visualized with FactoMineR v2.9(*57*). To run MrVi v0.2.0, the Seurat object was converted to h5ad with sceasy v0.0.7(*58*) and read as an AnnData object in Python. The MrVI model was trained following the tutorial. The sample-sample distances were predicted with MrVI (get_local_sample_representation) for each cell and then averaged over all cells. Sample-samples distances were visualized in a heatmap using pheatmap v1.0.12 in R (ward.D2,, euclidean distance measure).

Comparison with published datasets

We downloaded the publicly available annotated data from Yim et al.(*9*) (GEO GSE182098, sciatic nerve), Gerber et al(*10*), (https://snat.ethz.ch/seurat-objects.html, 10X Genomics P60), Mathys et al. (https://compbio.mit.edu/scBBB/ ROSMAP vascular cells)(*14*), and Wolbert et al. (*8*) (GEO GSE142541, mouse). If necessary, the data were preprocessed with Seurat, i.e. normalized with LogNormalize, highly variable genes were identified, scaled, and PCA was performed with default parameters. To identify novel marker genes, cell markers in the published datasets were determined with the FindMarkers function in Seurat (min.pct = 0.1, logfc.threshold = 0.25, p_val_ad < 0.05). To annotate our dataset based on the published dataset, rodent gene names were converted to orthologues using homologene v.1.4.68 (homologeneData2 database). We then classified our cells based on the annotated reference dataset using FindTransferAnchors and TransferData functions in Seurat with default parameters. Cells were labeled as unknown if the Seurat prediction score was below 0.3.

Histology: Semi-thin sections and analysis

After biopsy, ⅓ of the sural nerve was embedded in Epoxy resin (Fig. 1A, experimental setup). Semithin sections (1 µm) of sural nerves were cut using a EM UC7 ultramicrotome (Leica Microsystems) and stained with toluidine blue. The sections were scanned with a slide scanner (Münster/Würzburg: Grundium Ocus40; Essen: Zeiss Axio Scan Z.1, Hitachi HV F203SCL camera). After blinding, the entire number of total myelinated axons per sural nerve were counted manually by one investigator using the CellCounter plug-in of ImageJ v1.36. Physiologically unmyelinated axons (diameter <1 µm) and Remak- bundle fibers were not included.

The ImageJ g-ratio plugin was used to determine myelin thickness and axonal diameter of 15% of the total myelinated axons per sural nerve. In randomly chosen myelinated axons the inner and outer rim of a myelin sheath were manually traced by one investigator. The g-ratio was calculated by dividing the axonal circumference (i.e., inner rim of the myelin sheath) by the outer circumference of the respective myelin sheath, presuming circular axons. The g-ratio values of each patient were plotted against the calculated axon diameters.

Preparation of sural nerve cross sections and Xenium spatial transcriptomics

We created a custom stand-alone gene panel for spatial transcriptomics using the commercial Xenium Analyzer platform. The panel was designed based on our single nuclei analysis, mostly focussing on cells that demonstrated a potential role in polyneuropathies, including Schwann cells (mySc, nmSC, repairSC), perineurial cells and vascular cells such as pericytes and endothelial cells. We included a minimum of four top marker genes of each of the clusters and also defined twenty DE genes that were differentially expressed between the different PNP subtypes. We additionally included well known markers of both epi- and

endoneurial fibroblasts and different subtypes of leukocytes including B cells, T cells, and macrophages, adding up to a total of 99 genes (Suppl. Tab. 7).

In total, 8 sural nerve formalin-fixed paraffin-embedded (FFPE) samples were included for Xenium spatial transcriptomics: 2 CTRL (S22, S24), 2 CIDP (S01, S11), 2 CIAP (S04, S14) and 2 VN (S29, S30) samples (Suppl. Tab. 1). Samples were primarily selected based on their optimal/intact morphology in the semithin sections and their center with the aim to limit center bias..

Sample preparation and processing was carried out by the CMCB Technology Platform Core Facility EM and Histology and the DRESDEN-concept Genome Center at the Technical University Dresden, in Germany. Samples were processed according to manufacturer protocols (10x protocols, CG000580, CG00582 and CG00584). Briefly, 4 µm cross sections were collected, floated in a 37˚C water bath, and adhered to Xenium slides (10x Genomics, PN 1000460). Samples were deparaffinized in 2x Xylene and rehydrated in a descending series from 100% ethanol to MilliQ water. After inserting slides into xenium cassettes, samples were decross-linked and incubated overnight (22 hours) with padlock probes, followed by a post-hybridization wash. Subsequently, padlock probes were ligated, followed by rolling circle amplification, autofluorescence quenching, and nuclear staining (DAPI). Slides were loaded on a 10X Xenium Analyzer (software v. 1.6.1.0), for region selection, with each region corresponding to one entire nerve bundle.

Primary analysis, image processing and decoding, and secondary analysis, cell segmentation and transcript mapping, were performed on-instrument with the analysis software Xenium-1.6.0.8 resulting in a cell-feature matrix and an initial clustering. For cell segmentation, a custom neural network on DAPI images was initially used for nucleus segmentation. Then nucleus boundaries are expanded by 15 µm or until they encounter

another cell boundary in X-Y to define cell boundaries. Transcripts were mapped to these 2D shapes according to their X and Y coordinates. Gene expression mapping was visualized using the Xenium Explorer software v.1.3. The post Xenium H&E staining was processed according to the manufacturer protocol, including quencher removal in advance (see 10x Genomics protocol CG000613/A).

Xenium data analysis

Xenium data was loaded into Seurat. We removed cells with less than 10 molecules per cell. We performed normalization with SCTransform (default parameters) and computed PCA for each sample. To match our snRNA-seq data to our Xenium data, each cell was classified with the FIndTransferAnchors and TransferData function based on our previously annotated snRNA-seq data (downsampled to 1000 cells per cluster). Cells with a prediction score below 0.3 were labeled as unknown. The 24 main clusters were then aggregated into 8 larger groups (SC, endoC, periC, epiC, VSMC, PC, EC, IC). For manual quantification of endo- vs. epineurial transcripts the Xenium images were loaded into Xenium Explorer 1.3.0 (10x Genomics) and endoneurial areas were manually outlined using the selection tool while using visualization of Schwann cell marker transcripts (*EGR2, NGFR, SOX10, S100B)* to reliably identify such endoneurial areas. The area of each image visibly unoccupied by nerve-associated tissue was selected as epineurium. The area (in µm2), the number of total segmented cells, and the number of immune cell-associated transcripts (leukocytes: *PTPRC*/CD45, B cells: *MS4A1*/CD20, T cells: *CD3E*) was quantified and recorded in each selection area. The density of the respective transcript per total endorial and epineurial area were calculated for each sample. Selected transcripts were visualized in Xenium Explorer

1.3.0 (10x Genomics). Images were integrated with corresponding H&E staining to visualize the spatial orientation.